OMEGA Polar-Drive Target Designs

Introduction

With the use of polar drive (PD),[1] direct-drive experiments can be conducted at laser facilities such as the National Ignition Facility (NIF),[2] while they are configured for x-ray drive. In this approach to inertial confinement fusion, laser beams directly irradiate a capsule, causing the outer material to ablate and drive the rest of the shell like a rocket. Since the x-ray drive configuration has no beams at the equator, several modifications of traditional symmetric direct drive[3] are employed to achieve adequate symmetry. An important modification repoints beams from higher latitudes toward the equator, resulting in oblique irradiation on target. Laser-energy absorption of the expanding corona is dominated by collisional absorption, where maximum laser energy is deposited at the turning point of the laser rays. The electron density at the turning point of a laser ray scales as $\cos^2\theta$, where θ is the angle subtended by the laser rays. As a result, laser absorption occurs at lower coronal densities for larger values of θ, which correspond to the oblique beams.[1] This results in reduced shell velocity (or the hydrodynamic efficiency, defined as the ratio of the maximum shell kinetic energy to the incident laser energy), relative to when the beams are at normal incidence. Pulse-shape variations among the beams and tailored individual spatial-beam profiles are necessary to recover the shell velocity while achieving adequate shell symmetry. These variations are critical to the polar-drive–ignition design.[4] In the symmetric-drive configuration, the laser irradiation is incident from a range of latitudes including the equator. This results in more-normal incident laser irradiation and for a given ablator material, the maximum-possible energy deposited leading to maximum shell velocity.

Similar to symmetric drive, ignition in PD geometry relies on the formation of a hot spot with a minimum areal density of 300 mg/cm² and an electron temperature of ~5 keV. Assuming spherical symmetry, the adiabat and shell implosion velocity are the critical parameters that determine target performance. The minimum laser energy required for ignition, $E_{\min}$, has been shown to depend on α_{inn}, the adiabat on the inside of the compressing shell, defined as the ratio of the pressure to the Fermi-degenerate pressure, the velocity of the shell at

maximum kinetic energy or the implosion velocity V_{imp}, and the pressure P on the outside of the fuel when it reaches the implosion velocity:[5]

$$E_{\min}(\text{kJ}) = 50.8\,\alpha_{\text{inn}}^{1.88}$$

$$\times \left(\frac{V_{\text{imp}}}{3\times10^7\,\text{cm/s}}\right)^{-5.89}\left(\frac{P}{100\,\text{Mbar}}\right)^{-0.77}. \quad (1)$$

Equation (1) indicates that a lower adiabat on the inside of the shell, a high implosion velocity, and retaining the driving pressure on the outside of the shell until the onset of deceleration are extremely important to lowering the minimum energy required for ignition. The implosion velocity can be written as

$$V_{\text{imp}} \sim \sqrt{\langle\alpha\rangle^{0.6}\times\text{IFAR}\times 1^{0.27}}, \quad (\text{Ref. 6}) \quad (2)$$

where $\langle\alpha\rangle$ is the density-averaged adiabat in the shell, IFAR = R/Δ_{if} is defined as the ratio of the shell radius R to the shell thickness (Δ_{if} is defined as the distance between the $1/e$ radii of peak density) when the shell has traveled a distance that is 2/3 that of the average of the initial inner and outer target radii, and I is the on-target intensity. A higher implosion velocity can be obtained by increasing $\langle\alpha\rangle$, IFAR, or intensity.

The leverage in $\langle\alpha\rangle$ to increase V_{imp} is limited since it is challenging to increase $\langle\alpha\rangle$ and retain a low value of α_{inn}. Based on multidimensional considerations, IFAR has an upper limit because of nonuniformities seeded by the laser beams and target imperfections that can compromise implosion performance. Short-wavelength nonuniformities ($\ell \geq 10$, where ℓ is the Legendre mode number describing the nonuniformity) grow primarily by the Rayleigh–Taylor (RT) instability[7] and can significantly distort the in-flight shell, thereby increasing α_{inn} (Ref. 8). The number of linear growth factors for $\ell \geq 10$ for RT growth (defined as $N_e = \gamma t$, where γ is the RT growth rate and t is the time over which the shell accelerates) of the most dangerous mode (defined as the mode with wave number k, such that $k\Delta_{\text{if}} \sim 1$) scales approximately as $\sqrt{\text{IFAR}}$ (Ref. 9).

Too high an intensity can compromise target performance by seeding laser–plasma instabilities (LPI's) that reduce the energy coupled to the target (for example, through cross-beam transfer)[10] and/or preheating the shell and raising α_{inn} [via energetic electrons produced by two-plasmon-decay (TPD) instability].[11] As a result, the peak intensity, defined at the initial target radius, is typically restricted to $8 \times 10^{14} \lesssim I \lesssim 1 \times 10^{15}$ W/cm^2. At these intensities the effects of LPI are not completely understood.[12] Nonlocal heat transport by coronal electrons from the tail of the distribution function[13] also plays an important role in establishing the ablation pressure. It is necessary for OMEGA PD implosions to span this range of on-target intensities to permit studies relating to the heat conduction and LPI.

A second aspect of PD designs is the symmetry of the hot spot. Hot-spot symmetry is determined by longer wavelength perturbations ($\ell \leq 10$) that reduce the clean volume and decrease the hot-spot temperature, lowering the neutron yield.[14] In symmetric direct drive, hot-spot distortions are seeded by ice roughness, energy imbalance, beam-pointing variations, and beam-timing variations between the various beams incident on the target. The beam port configuration or beam geometry can cause additional hot-spot distortions to occur in PD.

Target performance, including the extension to multidimensional effects, has been quantified in a recent work by Haan *et al.* in terms of the ignition threshold factor (ITF).[15] A higher value of ITF indicates a greater probability of ignition; a value of 1 for this quantity indicates a 50% probability of ignition. ITF scales as

$$\text{ITF} \sim V_{\text{imp}}^8 \alpha^{-4} (1 - 1.2\,\sigma) \left(\frac{M_{\text{clean}}}{M_{\text{DT}}} \right), \qquad (3)$$

where σ is a measure of the hot-spot distortion given by the root-mean-square distortion of the hot spot, where longer wavelengths are weighted less than the shorter wavelengths, and $M_{\text{clean}}/M_{\text{DT}}$ is the ratio of the clean mass of the hot spot, i.e., the deuterium–tritium (DT) mass that is not contaminated by high-mode mixing of the ablator material, to the total target mass. High-mode mix caused by short-wavelength RT growth and the presence of isolated defects on the target surface is not considered in this article. The effect of this mix on target performance can be studied empirically through implosions by varying the IFAR, similar to what has been done in symmetric drive.[8] Engineering efforts to decrease the number of defects on the capsule surface are ongoing and have already resulted in improved implosion performance.[16] Modifications to the

target design through techniques such as radiation preheat[17] and the use of lower-density ablators such as foam[1] can be considered to limit the effect of short-wavelength RT growth. The emphasis in this article is on minimizing hot-spot distortion related to beam geometry on the OMEGA Laser System[18] and to establish the basis for ignition-relevant platforms that can be used to study LPI and heat conduction in PD geometry. In particular, this implies the identification of beam profiles that minimize hot-spot distortion in OMEGA PD designs with ignition-relevant parameters.

In symmetric drive, implosions are primarily designed in one dimension (assuming spherical symmetry) and then simulated in multiple dimensions to verify target performance. Since beam-port geometry has a very small effect on target performance in symmetric drive,[19] it can be ignored in the primary design. Beam profiles for OMEGA beams have been designed for symmetric drive by minimizing the nonuniformity related to the beam geometry when projected on a sphere.[20] This assumes that the laser deposition and hydrodynamic efficiency are uniform in polar angle around the target, valid for symmetric drive where the beams are nearly normally incident on the target. For polar drive, it is critical to account for the nonuniformities imposed by the beam-port geometry and to correct for them using techniques such as an optimal choice of beam profiles, beam pulse shapes, and beam repointing. The PD approach therefore requires iterative multidimensional simulations to design implosions.

Beam profiles are implemented on OMEGA using distributed phase plates (DPP's).[21] The intensity profile across the OMEGA beam, $I_b(x,y)$, is described by a super-Gaussian,

$$I_b(x,y) = I_0 e^{-\left(\frac{\sqrt{x^2 + y^2}}{\delta}\right)^n}, \qquad (4)$$

where n is the desired super-Gaussian order (approximately 3.7 for the existing phase plates on OMEGA[22]). The $1/e$ radius of the phase plates, δ, is determined by the relationship between the laser energy and target radius and the required scaling between NIF (1.5 MJ) and OMEGA (30 kJ) to conduct ignition-relevant symmetric drive studies on OMEGA ($\delta = 380\ \mu$m for the existing OMEGA Laser System[21]). For PD implosions, a smaller value of n is required to achieve greater irradiation control over localized regions of the target. This can effectively compensate for the reduced equatorial irradiation.

In OMEGA PD experiments, 40 of the 60 beams emulate the NIF x-ray–drive beam-port configuration. A subset of the

20 omitted drive beams at the equator irradiate a Ti/Fe foil to backlight the compressing shell to obtain information about its symmetry. The primary goal of OMEGA experiments is to validate models used to predict ignition. This implies that for low-adiabat implosions with relevant implosion velocities and on-target intensities, necessary models must be developed and simulations validated to reproduce experimental observables. Adiabat-related observables are primarily shock velocity,[23] areal density,[24] and bremsstrahlung radiation from energetic electrons produced from TPD that can potentially preheat the shell.[25] The implosion velocity is related to observations of neutron-production time[26] and scattered light[27] and is primarily determined by laser-energy coupling and heat conduction. Symmetry is inferred experimentally from backlit x-ray images of the converging shell[28] and is determined by adiabat, implosion velocity, and nonuniformity growth. An additional useful metric of PD target performance is the comparison of PD and symmetric-drive implosions at the same laser energy and adiabat.

Current OMEGA warm PD implosions[29] are irradiated with approximately 13 kJ on target at a relatively low intensity at the initial target radius ($\sim 3.5 \times 10^{14}$ W/cm^2). The low-intensity values are driven primarily by the available energy for PD. Since 40 of the 60 beams are used, only 2/3 of the available energy is used to drive the capsule, resulting in low on-target intensity. In this article, we first present cryogenic designs for the existing system that predict implosion velocities of 3.6×10^7 cm/s at low on-target laser intensity. We then present higher-intensity PD designs that use smaller targets ($R_{target} = 300$ μm) driven with smaller custom laser-beam profiles (with a $1/e$ radius of ~ 183 μm or a

radius at 5% of peak intensity of 300 μm), with lower values of the super-Gaussian order ($n = 2.2$) and elliptical beam profiles for the equatorial beams. This results in a higher on-target intensity, at the initial target radius, of $\sim 9 \times 10^{14}$ W/cm^2, allowing for LPI and heat-conduction studies.

In the next section, cryogenic-DT polar-drive–implosion designs are presented for the current OMEGA system. It is predicted that the PD implosions will result in reduced implosion velocity relative to symmetric drive implosions at the same energy by $\sim 10\%$. Observations from warm (CH) implosion related to a similar loss of implosion velocity in PD relative to symmetric drive are also presented in the next section. In the following sections, a PD cryogenic deuterium–tritium (DT) design is presented at ignition-relevant intensities with smaller targets. The sensitivity of these designs to beam profiles is also studied. In addition, a warm plastic (CH) design with ignition-relevant intensities is presented. Observations related to an additional loss of $\sim 10\%$ in PD implosion velocity relative to simulations that include only collisional absorption are discussed and the conclusions are presented.

Low-Intensity Designs for the Current OMEGA Laser System

OMEGA cryogenic-DT implosion designs using laser beams with a super-Gaussian profile of $n = 3.7$ are presented here. The NIF beam configuration [Fig. 130.1(a)] is emulated by using 40 of the 60 OMEGA beams arranged in three rings [Fig. 130.1(b)]. Beams from the higher latitudes are repointed toward the equator in the PD configuration to achieve adequate symmetry [Fig. 130.1(c)]. This is equivalent to each beam in an
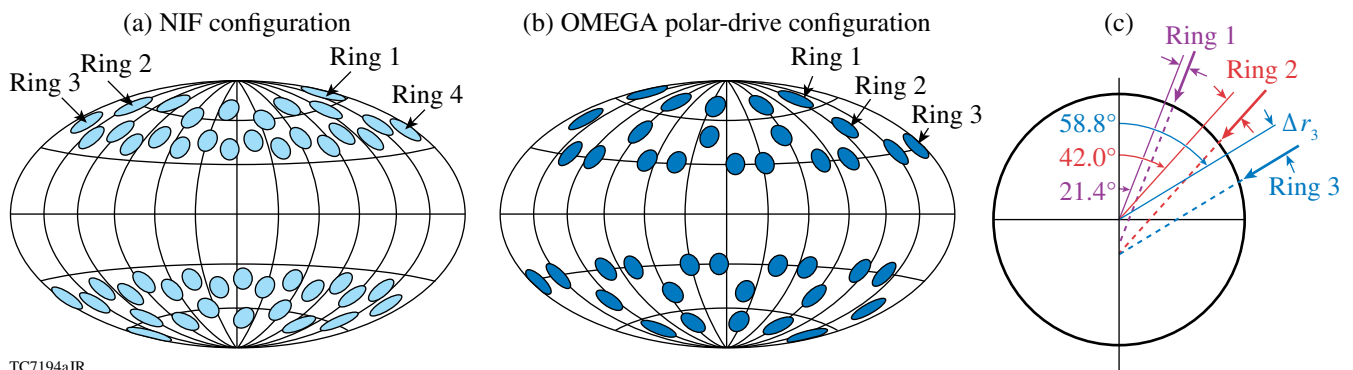

Figure 130.1
(a) NIF beam configuration. (b) Forty of the 60 OMEGA beams, arranged in three rings, emulate the NIF beam configuration. (c) Each ring is repointed by a distance (Δr_3 is shown as an example for Ring 3) toward the equator to improve symmetry. Solid lines—original beam pointing; dashed lines—repointed beams.

OMEGA ring being displaced by a distance Δr perpendicular to the beam axis. Each PD configuration is described by three distances (Δr_1, Δr_2, Δr_3) or equivalently by three angles:

$$\left[\sin^{-1}\left(\Delta r_1 / R_{\text{target}}\right), \sin^{-1}\left(\Delta r_2 / R_{\text{target}}\right), \sin^{-1}\left(\Delta r_3 / R_{\text{target}}\right)\right].$$

The latter description is advantageous because it is independent of the target radius and allows for comparison of OMEGA- and NIF-scale designs. To allow one to make a comparison with previous OMEGA PD work,[28,29] both descriptions are retained here. Implosions are simulated with the two-dimensional (2-D) axisymmetric radiation hydrodynamic code *DRACO* using multigroup diffusive radiation transport and flux-limited heat conduction.[19] A full three-dimensional (3-D) ray trace that uses collisional absorption to deposit the laser energy[30] is employed to accurately model laser ray trajectories of the oblique beams.

The design of a PD implosion begins with a symmetric design that is then iteratively optimized using *DRACO*. Parameters of the 60-beam symmetric design (design A), simulated with collisional absorption and a flux-limited ($f = 0.06$) heat-conduction model, using the spherically symmetric code *LILAC*,[31] are shown in Table 130.I. The laser pulse shape has three pickets followed by a main pulse. This pulse shape has been used to demonstrate a high areal density of nearly 300 mg/cm^2 in previous cryogenic implosions.[32] The PD ignition design[4] also uses a pulse shape

of this type. The maximum-possible OMEGA laser energy in the PD configuration is used in this design. This design has an ignition-relevant adiabat implosion velocity and an IFAR comparable to an ignition design value of 36 (Ref. 4). The convergence ratio at bang time is 20, comparable to the ignition design value of 23. The overlapped-beam intensity at the initial target radius is 4.2×10^{14} W/cm^2. While the intensity defined at the initial target radius provides a useful rule of thumb in defining the relevant range for target designs, the physically more-relevant quantity is the intensity at the quarter-critical surface. The quarter-critical intensity $I_{n/4}$ is somewhat less than the intensity at the initial target radius because of absorption in the lower-density corona. For this design, this value is 3×10^{14} W/cm^2, which is significantly lower than the values in the ignition design ($\sim 8 \times 10^{14}$ W/cm^2). Consequently, the TPD threshold parameter, defined as

$$\eta = I_{n/4}\left(10^{14}\ \text{W/cm}^2\right)L_{n/4}(\mu m)\Big/233\,T_{n/4}^{\text{e}}(\text{keV})\ \text{(Ref. 11)},$$

where $L_{n/4}$ and $T_{n/4}^{\text{e}}$ are the density scale length and the electron temperature at the quarter-critical surface, respectively, is less than 1, indicating a marginal effect of TPD on electron generation and capsule preheat.[33]

A 40-beam PD implosion with the same energy, based on this design, is optimized using *DRACO* (Fig. 130.2). In the PD case, the single-beam energies are increased by 3/2 to ensure

Table 130.I: Parameters of 60-beam, symmetric-drive OMEGA cryogenic-DT designs simulated with collisional absorption and flux-limited heat conduction. Polar-drive optimization using the 2-D axisymmetric hydrodynamics code *DRACO*[19] is based on these designs (see text).

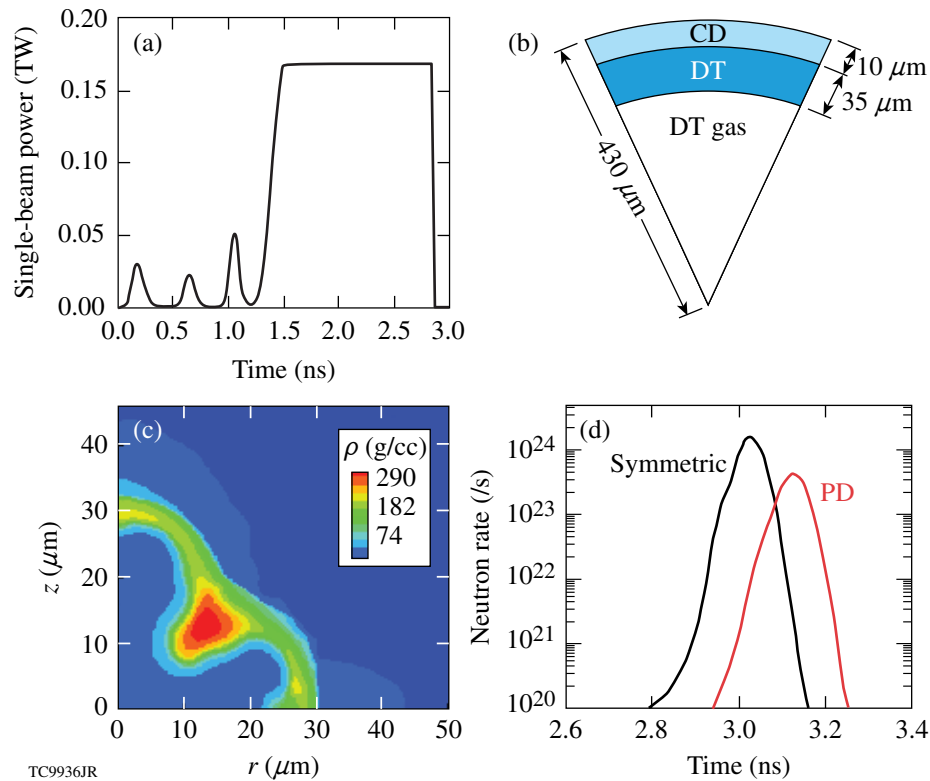|	Design A	Design B	Design C
R_{outer} (μm)	430	300	300
Ice thickness (μm)	35	35	65
CH ablator (μm)	9	9	9
Peak power (TW)	10	10	10
E (kJ)	15.5	11.5	12.8
V_{imp} (cm/s)	3.6×10^7	3.4×10^7	2.5×10^7
IFAR	32	22	12
DT yield	1.2×10^{14}	2.7×10^{13}	5.0×10^{12}
ρR_{max} (mg/cm^2)	243	240	236
R_{hs} (μm)	20	15	15
CR	20	17	15
$L_{n/4}$ (μm)	150	110	110
$I_{n/4}$ (W/cm^2)	3×10^{14}	7×10^{14}	7×10^{14}
$T_{n/4}^{\text{e}}$ (keV)	2.1	2.8	2.8
$\eta_{\text{TPD}} = I_{n/4}\left(10^{14}\ \text{W/cm}^2\right)L_{n/4}(\mu m)\big/233\,T_{n/4}^{\text{e}}(\text{keV})$	0.9	1.3	1.3

Figure 130.2

(a) Pulse shape and (b) target for cryogenic DT polar-drive (PD) design on the existing OMEGA Laser System with $n = 3.7$ phase plates. (c) Mass-density profiles at peak neutron production. (d) Neutron-rate histories—symmetric drive (black) and PD (red).

that the target is irradiated with the same total picket energies and total energy [Fig. 130.2(a)]. This PD configuration corresponds to beam ring displacements of 90 μm, 150 μm, and 150 μm. As the density contours at peak neutron production [Fig. 130.2(b)] indicate, the core has a small $\ell = 2$ and a large $\ell = 4$. The implosion velocity for the PD design is approximately 10% less than that of the symmetric design. Bang time, defined as the time of the onset of the neutron yield above the experimental noise threshold, is an important observable to quantify the implosion velocity. For the typical temperatures in these implosions, neutron rate Y_{1n} scales with mass density ρ and the fusion reaction rate as ion temperature T_i of the fuel as $Y_{1n} \sim \rho^2 \langle \sigma v \rangle d^3 r$, where $\langle \sigma v \rangle \sim T_i^4$. Using $T_i \sim \alpha^{-0.15} V_{imp}^{1.3}$ (Ref. 9), the neutron rate can be written in terms of implosion velocity as $Y_{1n} \sim \rho^2 \alpha^{-0.6} V_{imp}^{5.2}$. The measured rate can deviate from this one-dimensional (1-D) formulation because the growth of nonuniformity can reduce both T_i and the neutron-producing volume (or "clean volume"). Simulations indicate that nonuniformity does not significantly influence the rate in these implosions early during the deceleration phase. Therefore comparing the bang time provides a measure of the implosion

velocity. This reduced velocity is shown as the delay in neutron-production history in Fig. 130.2(c).

Additional variables, including beam energies and shimming, can be employed to optimize the design. The best symmetry for the PD equivalent of design A is obtained with only beam displacements. Beam profiles are predetermined and no combination of beam energies and displacement can improve upon the symmetry of the design shown in Figs. 130.2(a) and 130.2(b). Since it is challenging to achieve adequate equatorial drive in the PD configuration, thinning the DT ice or ablator near the equator or shimming may improve the density uniformity locally near the equator. This is not studied in this work.

The final optimized PD design typically differs somewhat from the original symmetric design because of the retuning of the shocks to achieve adequate uniformity and timing with oblique beams. Since the difference in peak areal density between the original symmetric design (design A) and the PD-optimized design is less than 5%, the original design A is retained as the symmetric equivalent of the optimized PD

design. The predicted PD yield is 27% of the symmetric-drive yield. This reduction is due to the $\ell = 4$ nonuniformity and the reduced implosion velocity in PD relative to symmetric drive. These predictions are similar to observations from warm CH PD implosion experiments.

In warm PD OMEGA implosion experiments, triple-picket laser pulse shapes (Fig. 130.3) irradiate a 9-atm-deuterium-filled, 27-μm-thick CH shell with approximately 13 kJ of laser energy. Full beam smoothing [smoothing by spectral dispersion (SSD)][34] and polarization smoothing (PS)[35] are used in all of the implosions. These implosions are designed to achieve a convergence ratio (CR) of 19, where CR is defined as the ratio

TC9634JR

Figure 130.3
(a) Laser pulse shape used to irradiate the target shown in (b) in current OMEGA polar-drive experiments.

of the initial inner shell radius to the hot-spot radius (defined as a radius that is $1/e$ of peak density) at peak neutron production. It has been shown previously[29] that very good agreement in picket shock velocities and catch-up at the equator is obtained in PD geometry as measured through VISAR (a velocity interferometer system for any reflector)[23] and simulated with *DRACO*.[19] Approximately 100% of the predicted value of areal density (ρR), measured through the energy loss of charged particles,[24] is obtained in these implosions. Since $\rho R \sim \alpha^{-0.6}$ (Ref. 36), this indicates that the predicted adiabat is achieved in the implosion. By comparing the simulated and measured neutron-production time ("bang time" is defined as the time when the neutron rate rises above the experimental noise level), it is estimated that simulations overpredict implosion velocity by ~10%. This will be discussed in the context of CBET (cross-beam energy transfer). The predicted shell asymmetry was well reproduced in these implosions,[29] until the shell converged by a factor of only 7, the latest time at which shell nonuniformity can be reliably inferred from experimental images.

The ratio of PD yields to the equivalent energy symmetric-drive yields versus the on-target laser energy is shown in Fig. 130.4(a) for different PD configurations. The average experimental symmetric drive yield is $(1.2\pm0.2) \times 10^{10}$ (averaged over four shots) compared to an average simulated value of $(1.12\pm0.3) \times 10^{11}$. The experimental reduction in the symmetric drive yield is due to nonuniformities such as beam imbalances, including primarily beam mistiming and target-surface rough-
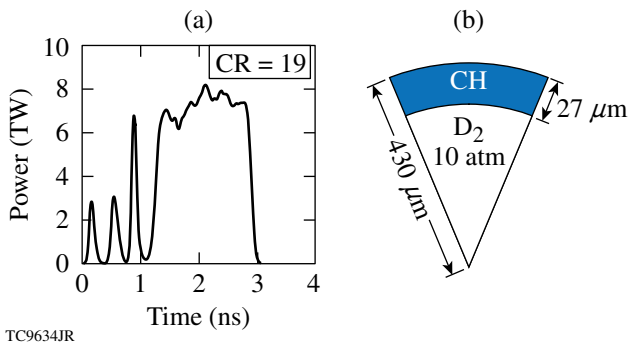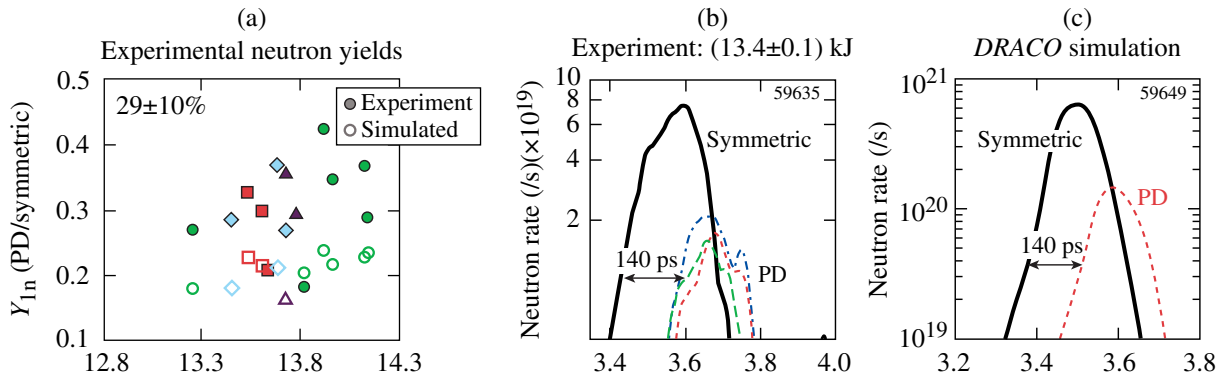

Figure 130.4
(a) Ratio of D_2 neutron yield from PD implosions to symmetric-drive implosions versus laser energy. Each symbol represents a shot. Solid circles represent experimental ratios for PD and symmetric-drive implosions; open circles represent simulated ratios for PD and symmetric-drive implosions. PD configurations are 90 μm, 120 μm, and 120 μm (circles); 90 μm, 150 μm, and 150 μm (squares); 90 μm, 133 μm, and 133 μm (triangles); and 30 μm, 150 μm, and 150 μm (diamonds). The average experimental ratio is 29±10% compared to the average simulated ratio of 20±10%. (b) Measured symmetric drive (solid) neutron rate compared to measured PD (dashed) neutron rates. Different curves correspond to different shots. (c) Simulated neutron rate for symmetric drive (solid) compared to simulated PD (dashed) neutron rate.

ness. Polar-drive yields are further reduced from the symmetric drive yields. The average reduction in the experimental ratio [Fig. 130.4(a)] is (29±10)% compared to the simulated reduction of (20±11)%, which is in good agreement.

The delay in the PD bang time relative to symmetric drive is evident from Fig. 130.4(b). Experimentally the (140±50)-ps delay in the PD bang time relative to the symmetric drive bang time requires a reduction of about 10% in the implosion velocity relative to symmetric drive. Simulations reproduced this delay in bang time [Fig. 130.4(c)]. Using the scaling of the neutron rate with the implosion velocity presented earlier, nearly 80% improvement in the absolute PD neutron yield can be achieved by increasing the implosion velocity by 10%.

The four experimental PD configurations correspond to beam distance displacements of 90 μm, 120 μm, and 120 μm; 30 μm, 150 μm, and 150 μm; 90 μm, 150 μm, and 150 μm; and 90 μm, 133 μm, and 133 μm. The extent of beam repointing in all these configurations is quite significant and results in reduced energy deposited (these repointed configurations also have a significant amount of energy that misses the target, contributing to the reduced energy deposition) and, therefore, reduced hydrodynamic efficiency. To compare these values with those in the NIF ignition design, these numbers are converted to scale invariant angles corresponding to 12°, 16°, and 16°; 4°, 20°, and 20°; 12°, 20°, and 20°; and 12°, 18°, and 18°.

The NIF ignition design also significantly repoints the beams—corresponding to 1.5°, 14.5°, 0°, 38.5°, and 33° for each ring on the NIF,[4] respectively. However, individual laser-spot profiles are optimally designed to prevent energy from going over the horizon of the target; beams are truncated asymmetrically, so that only insignificant beam energy misses the target. Moreover, sufficient energy is available on the NIF to compensate for the reduced hydrodynamic efficiency. Asymmetrically truncated beam profiles are not currently available on OMEGA and, as will be pointed out later, are also not practical for future OMEGA designs. For OMEGA-scale implosions, where the energy is limited, recovering this implosion velocity is important for studying the relative performance of PD and symmetric drive. Better control over the energy deposition in polar angle over the target, by choosing a different spatial beam profile, can make it possible to recover the implosion velocity in OMEGA-scale implosions, as discussed in the next section.

High-Intensity OMEGA Designs

Beam profiles with a relatively high super-Gaussian (SG) order result in a broad deposition region over the target. The spatial beam profiles from individual beams are compared for two different SG orders with $\delta = 383$ μm in Fig. 130.5. The higher SG order ($n = 3.7$) is characterized by a flat-top in intensity distribution, whereas the lower SG order ($n = 2.2$) is more center peaked. This center-peaked distribution allows for more-localized on-target intensity when the overlap of all beams within a ring is considered. As a result, the laser irradiation can be more effectively pointed toward the equator with the lower SG order (Fig. 130.6). For the $n = 3.7$ beam profiles currently on OMEGA, the overlapped-intensity distribution from each ring is broadly incident over a large range of polar angles [Fig. 130.6(a)]. The normalized overlapped intensity (normalized to the maximum value among the three rings, which corresponds to the Ring 1 intensity at the pole) is shown in Fig. 130.6(a) for the un-repointed beam configuration. With the lower SG order, again, for the un-repointed configuration, particularly for Rings 2 and 3, the intensity distribution on target is more peaked toward the equator [Fig. 130.6(b)]. The overlapped intensities from each ring are compared when the beams are repointed [Figs. 130.6(c) and 130.6(d)]. The beam displacements correspond to (16 μm, 21 μm, 68 μm) or (3°, 4°, 13°) values that result in optimized designs, as will be shown below. The equator is under driven by nearly 20% relative to the pole for $n = 3.7$ [Fig. 130.6(c), dashed lines], whereas the $n = 2.2$ beam profiles permit nearly the same intensities at the equator and pole [Fig. 130.6(d), dashed lines]. A purely elliptical beam profile described by

$$I_b(x,y) = I_0 e^{-\left[\frac{\sqrt{\eta_3 x^2 + y^2}}{\delta}\right]^n} \tag{5}$$

with ellipticity $\eta_3 = 1.2$ for Ring 3 permits greater intensity at the equator relative to a purely circular beam profile in both
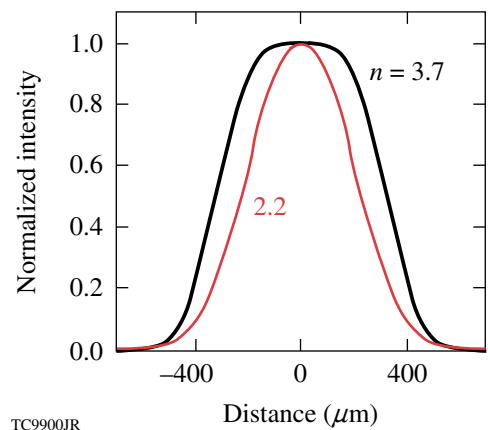

Figure 130.5
Beam profiles for two different super-Gaussian orders: $n = 3.7$ (black) and $n = 2.2$ (red).
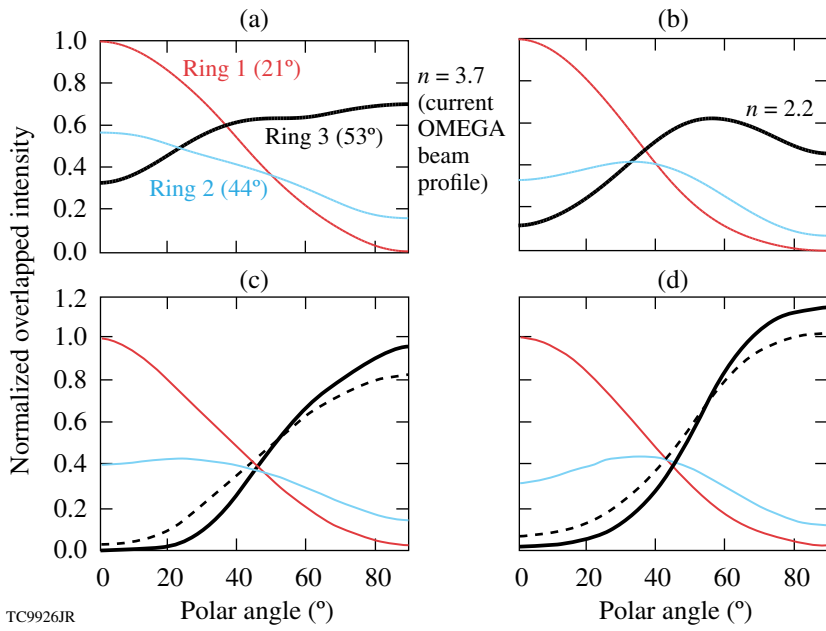
TC9900JR

Figure 130.6
On-target normalized overlapped beam intensity attributed to each OMEGA ring versus polar angle: (a) $n = 3.7$ and (b) $n = 2.2$. A lower super-Gaussian order provides a more-localized intensity pattern toward the equator (polar angle = 90°). (c) Overlapped on-target normalized beam intensity attributed to each OMEGA ring versus polar angle for the repointed configuration (16 μm, 21 μm, 28 μm) when only circular $n = 3.7$ beam profiles are used for all rings (solid), when an elliptical profile is used only for Ring 3 with ellipticity $\eta_3 = 1.2$ (dashed), and (d) only circular $n = 2.2$ beam profiles are used for all rings (solid), elliptical profile only for Ring 3 with ellipticity $\eta_3 = 1.2$ (dashed).

cases (solid line). With the same beam displacement, the lower SG order with elliptical beam profiles for Ring 3 is the more-favorable option to compensate for the reduced equatorial drive. This combination irradiates the equator with higher intensity than the pole by nearly 20% compared to the higher SG order.

To increase on-target laser intensity closer to ignition-relevant values, an appropriate value of δ and target radius (R_{target}) is required. The goal is to irradiate the target with NIF-relevant laser quarter-critical intensity. There is no simple scaling argument for the quarter-critical intensity when two different target sizes and laser energies are compared. The NIF target radius is 3 to 4 times that of an OMEGA-scale target, resulting in a proportionately longer coronal density scale length. More absorption occurs in the lower-density corona in the NIF designs because of the longer scale length, leading to a different dependence for the quarter-critical intensity on the

incident laser intensity in the NIF designs versus the OMEGA designs. Dimensional scaling relating the required laser energy for a given plasma energy is used as a starting point for a target radius. This is then iteratively adjusted to achieve similar simulated quarter-critical intensity in both designs. Using the scaling for the laser energy E contributing to a given plasma energy, $E \sim R^3$, and typical NIF and OMEGA parameters $R_{NIF} = 1700\ \mu$m, $E_{NIF} = 1.5$ MJ, and $E_\Omega^{PD} = 12$ kJ, one gets $R_\Omega^{PD} = 350\ \mu$m. If one instead uses a 15% smaller target radius, the intensity at the quarter-critical surface will increase from 4.5×10^{14} W/cm^2 to 6.5×10^{14} W/cm^2 [Fig. 130.7(a)], a value closer to the PD ignition design value, which varies between 7 and 9×10^{14} W/cm^2 in the polar angle on target [Fig. 130.7(b)]. Higher intensities in the OMEGA designs can be obtained by increasing laser energy (an additional 20% is available for the design as described below) or by further reducing the target radius. The latter approach typically results in lower convergence and is therefore not preferred.
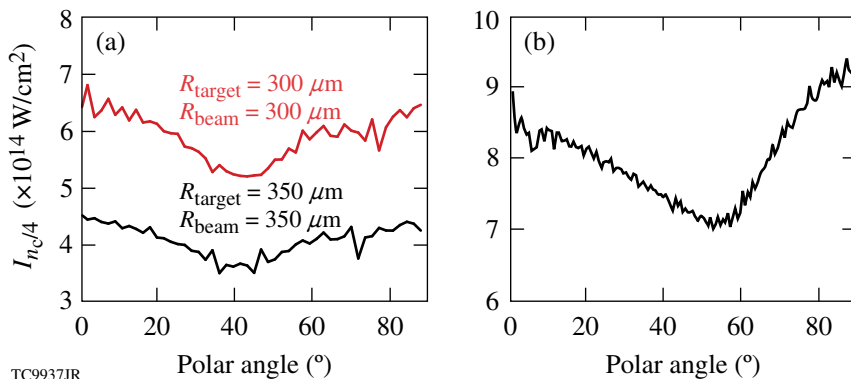

Figure 130.7
(a) Overlapped on-target intensity at the quarter-critical surface at the end of the laser pulse for two different target radii. The beam radius equals the target radius in each case. (b) Overlapped on-target intensity at the quarter-critical surface for the NIF design.[4]

Parameters for the 60-beam OMEGA cryogenic-DT symmetric target designs are shown in Table 130.I. The target has a radius of 300 μm with a 35-μm-thick (design B) or 65-μm-thick (design C) DT layer inside a 9-μm-thick CH shell. This CH thickness is chosen so that only CH is present throughout the laser pulse at the quarter-critical surface in the corona. The presence of DT at the quarter-critical surface is associated with a greater production of energetic electrons from TPD, which can potentially preheat the target.[37] The 65-μm layer thickness corresponds to ongoing symmetric-drive OMEGA cryogenic-DT experiments.[16] With the smaller target radius, initial experiments will be performed using this thicker, more-stable shell. This design deliberately uses only about 80% of the laser energy available on OMEGA; this can be increased by increasing either the intensity, the length of the pulse, or the relative energies of the rings. It is important to note that OMEGA experiments with ignition-relevant intensities are possible at this target radius. The smaller target radius results in a smaller convergence ratio for designs B and C. This can be increased by decreasing the shell adiabat by selecting a main pulse with a step as in Ref. 32. At the values of $I_{n/4}$ accessible in these designs, the TPD threshold parameter η_{TPD} exceeds 1 and has values similar to those in current symmetric-drive OMEGA experiments.[38]

Parameters of the PD design corresponding to the symmetric design C are summarized in Table 130.II. In PD, Ring 3 has 25% more energy than Rings 1 and 2 (parameterized by the variable E_{mod}). An elliptical beam profile [Eq. (5)] is chosen for Ring 3, increasing the equatorial drive (Fig. 130.8). The mass-density profile in Fig. 130.9(a) shows the shock as it breaks out of the DT layer for the 65-μm-thick DT design. The shock front is nonuniform, with the equator being somewhat underdriven compared to the rest of the target. The density contours at peak neutron production indicate a fairly uniform shell [Fig. 130.9(b)]. Little evidence of the underdriven equator is observed at peak neutron production because of shock dynamics. The return shock at the equator is weaker than the shock elsewhere. As a result, the shell at the equator travels a greater distance before it decelerates. Ideally, PD target design should optimize different phases of the implosion. In the NIF design, this is achieved by varying the pulse shapes of each ring independently in time. Picket energies vary between rings relative to the energy in the main pulse to ensure uniformity throughout the implosion. Only overall beam energies can be varied on OMEGA; therefore, only an overall optimization of the implosion is possible.

When beam energies are varied, the equivalency of sym-

Table 130.II: Parameters for the nominal high-intensity PD cryogenic OMEGA implosion based on design C in Table 130.I. E_{mod} is the overall energy multiplier to the pulse shape for Design C in Table 130.I; n is the super-Gaussian order for the rings; δ is the $1/e$ radius of the beam profile [Eq. (5)], η is the ellipticity of the beam profiles defined as the ratio of the major to minor axis of the beams (Eq. 5); and Δr is the extent to which the beams are repointed.

	Ring 1	Ring 2	Ring 3
E_{mod}	1.00	1.00	1.25
n	2.2	2.2	2.2
δ	183 μm	183 μm	183 μm
η	1.0	1.0	1.2
Δr	16 μm	21 μm	68 μm
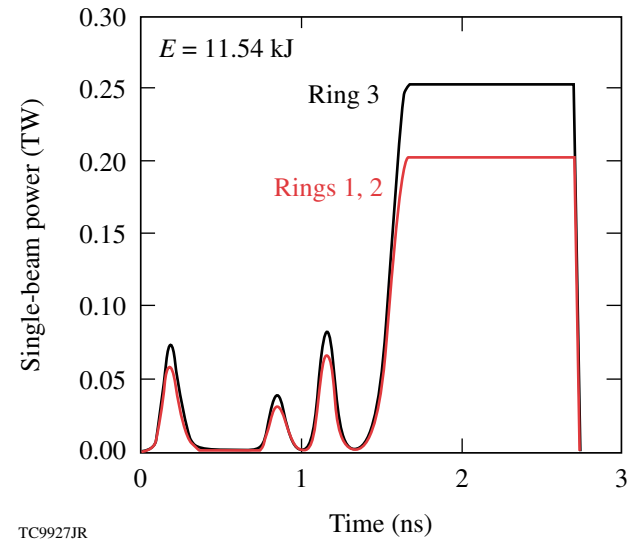
TC9927JR

Figure 130.8
Cryogenic target design used with the beam repointing in Fig. 130.6. Laser pulse shapes used for each of the rings irradiating the target in design C.

metric drive and PD implosions is less apparent. Here, since Ring 1 is nearly normally incident and the variations in pointing and beam energies relative to symmetric drive for the other rings are used to correct for beam obliquity, Ring 1's picket energies correspond to the equivalent symmetric-drive pulse shape for the optimized PD design. These are the same energies as the original symmetric design C. The peak power in the PD-equivalent symmetric design is appropriately chosen to keep the overall laser energy constant. Nearly 1-D areal density is achieved with a peak-to-valley variation of less than 10% [Fig. 130.10(a)]. The PD design obtains the same bang time as
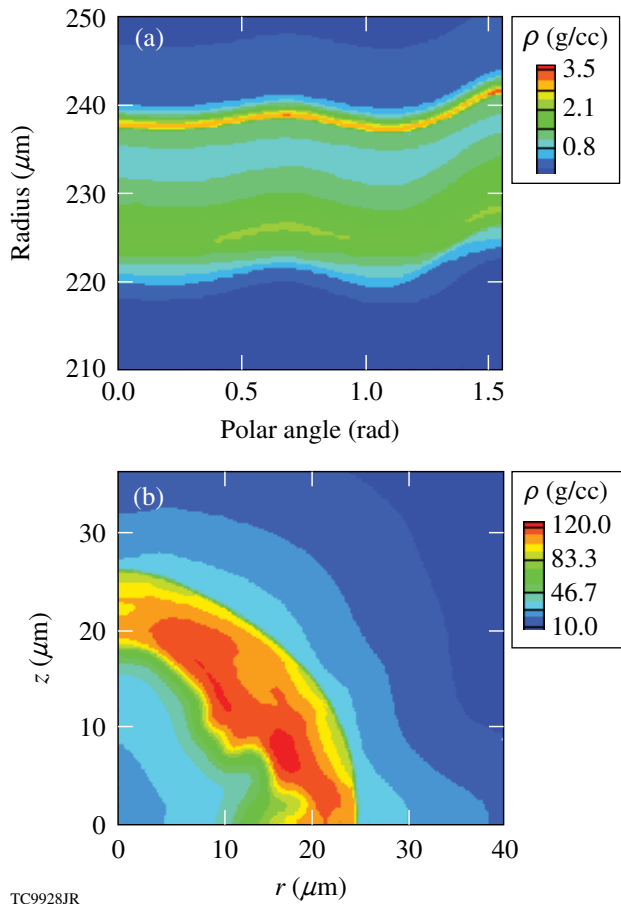
TC9928JR

Figure 130.9

(a) Mass-density contours shortly after shock breakout (1.7 ns) for the design in Fig. 130.8 with parameters in Table 130.II. (b) Mass-density contours at peak neutron production (2.8 ns) for the target design shown in Fig. 130.7.

the symmetric design, indicating that the symmetric drive's hydroefficiency is achieved in the PD design [Fig. 130.10(b)]. Nearly 55% of the symmetric drive's yield is obtained in the PD design. This reduction in PD yield is due to the residual nonuniformity, primarily $\ell = 4$.

The OMEGA beam profiles differ from the NIF beam profiles in two respects: The NIF design uses a circular spot modulated by an offset ellipse to provide greater uniformity locally near the equator. In the OMEGA design a similar spot for Ring 3 eliminates the weaker shock near the equator [Fig. 130.9(a)]. This spot is impractical on OMEGA, however, given the dispersion required by SSD. The extent of SSD dispersion (~180 μm) is comparable to the minor radius of the required ellipse, which then necessitates an extremely small (~10 μm) sized pre-SSD ellipse. Such a variation in intensity is impractical to manufacture through a phase plate. The second source of difference is in the beam truncation scheme employed in the NIF design. NIF beam profiles are asymmetrically truncated such that the laser energy spilling over the target horizon is minimized. This allows more energy to couple to the target. On OMEGA, however, this truncation is unnecessary. OMEGA designs require less repointing to achieve optimal symmetry because the beam-port arrangement on OMEGA is more optimal and the smaller-scale targets provide better hydrodynamic efficiency. Beam truncation is required when the repointing is significant since it permits adequate irradiation of the equator without loss of laser energy over the horizon. The optimal beam repointing on OMEGA is small enough that the effect of beam truncation is a simulated unobservable increase of ~2% in the implosion velocity.
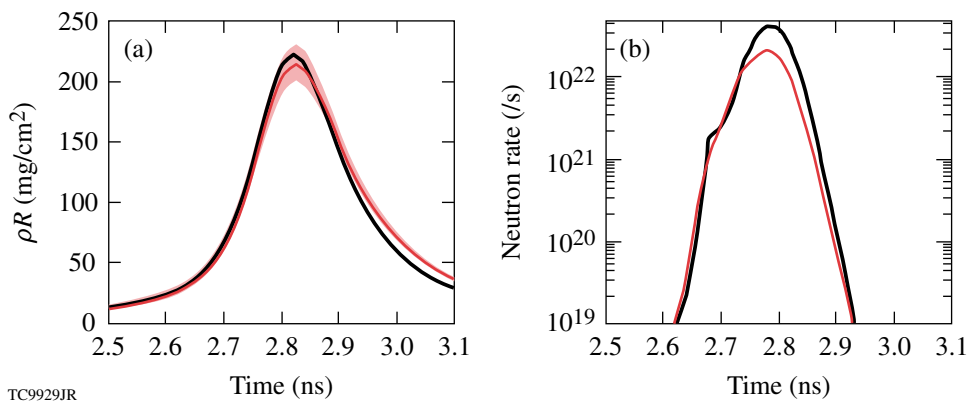

TC9929JR

Figure 130.10

(a) Areal-density history for symmetric drive (black) compared to the PD implosion (red). The shaded region indicates the range in areal densities in polar angle. (b) Neutron rate for symmetric drive (black) compared to PD (red). No significant difference in neutron-production timing is calculated indicating that the symmetric-drive implosion velocity is achieved in the PD simulation.

Sensitivities to the OMEGA beam profiles are investigated by systematically varying their parameters (Fig. 130.11). Hot-spot distortion, defined here as the ratio of the standard root-mean-square deviation of the hot-spot radius (defined as the inner $1/e$ location of peak density) to the mean hot-spot radius is used as a measure of implosion quality. This quantity is further broken down into the contribution from the various modes; the ratio of the amplitude of an individual mode to the hot-spot radius is also shown in Fig. 130.11. Super-Gaussian orders of each of the rings and the ring ellipticity are varied individually. As Fig. 130.11 indicates, Legendre modes with $\ell = 2$ and $\ell = 4$ dominate hot-spot distortion. For 10% variations in the SG order, no significant variation in target performance is observed, indicating the robustness of the design. Neutron yields do not change significantly when the beam profile parameters are varied. The parameter that is most sensitive to implosion quality is the ellipticity of the Ring 3 beams' profiles. For Ring 3 ellipticity, the most-sensitive determinant of implosion quality, the neutron yield relative to symmetric drive varies between 58% (for $\eta_3 = 1.0$) and 54% (for $\eta_3 = 1.25$) (see Fig. 130.12).
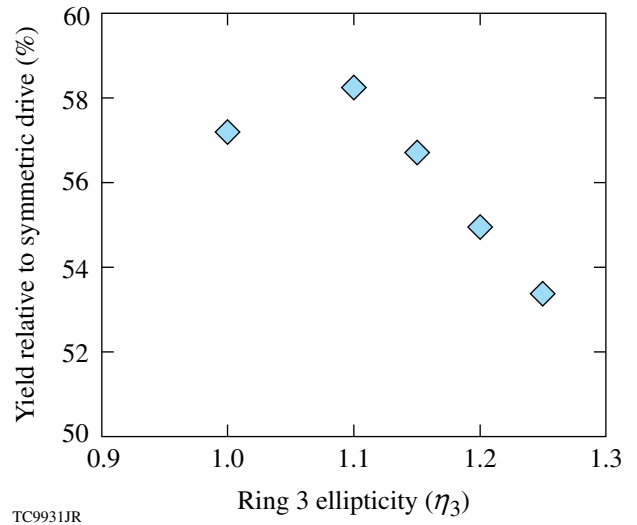

TC9931JR

Figure 130.12
Yield relative to symmetric drive versus Ring 3 ellipticity. The PD yield for $\eta_3 = 1.15$ coresponds to 2.3×10^{12}, whereas the symmetric drive yield is 4×10^{12}.
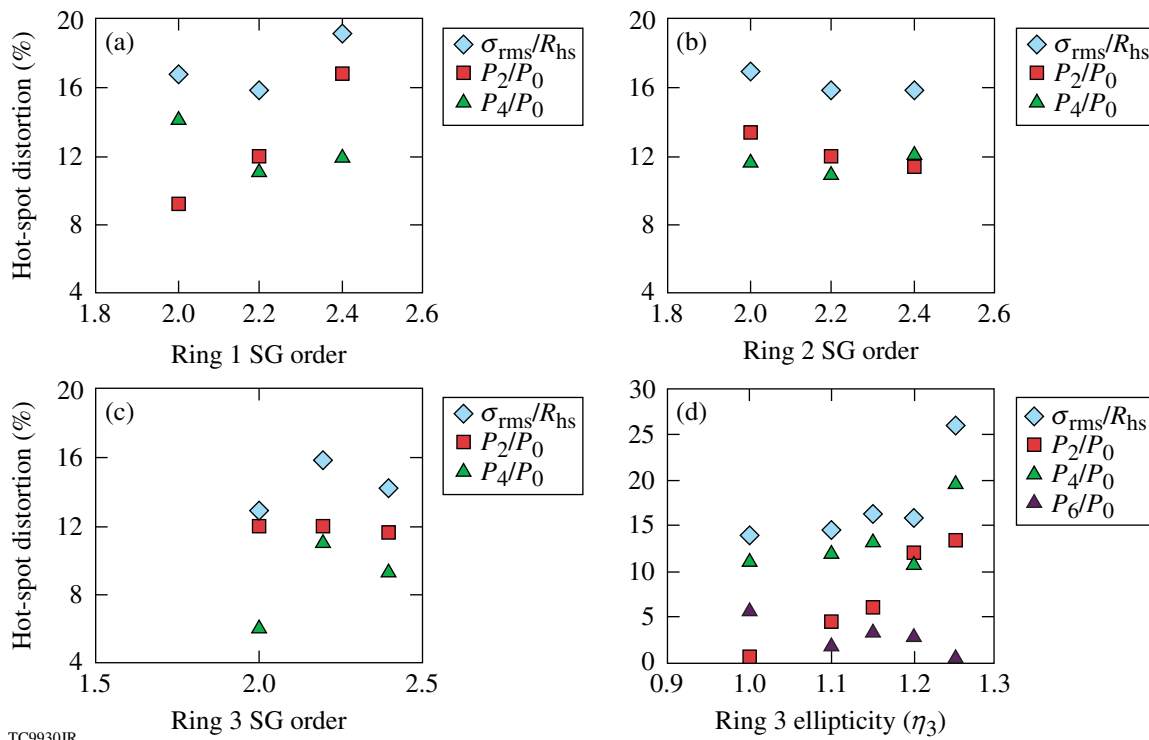

TC9930JR

Figure 130.11
(a) Sensitivity of hot-spot distortion to super-Gaussian (SG) order of Ring 1 beams; (b) sensitivity of hot-spot distortion to super-Gaussian order of Ring 2 beams; (c) sensitivity of hot-spot distortion to super-Gaussian order of Ring 3 beams; (d) sensitivity of hot-spot distortion to ellipticity of Ring 3 beams, η_3. Diamonds: ratio of σ_{rms} of hot spot to radius of hot spot (R_{hs} is defined as the $1/e$ of peak density); squares: ratio of amplitude of Legendre-mode P_2 to R_{hs}; green triangles: ratio of amplitude of Legendre-mode P_4 to R_{hs}; dark purple triangles: ratio of amplitude of Legendre-mode P_2 to R_{hs}.

Manufacturing uncertainties introduce variability among phase plates. Such variations can cause the on-target intensity profile to deviate from the pure Legendre mode assumptions used in the design. To constrain the range of acceptable beam profiles, simulations are performed with varying ellipticity for Ring 3 beams. A randomly selected ellipticity for each beam in Ring 3, with η_3 varying uniformly between 1.1 and 1.2, is used in the simulations. The effect of varying ellipticities is bracketed by two different models of the nonuniformity (Fig. 130.13): (1) Only the $m = 0$ modes in the Legendre decomposition of the asymmetry in the 2-D axisymmetric simulation are used as the initial perturbation amplitudes. (2) The amplitude of the $m \neq 0$ modes is added in quadrature to reach the amplitude of the Legendre mode used in the simulation, where the effect of the 3-D perturbation introduced by beam profile variations can be approximated. The middle point, $\eta_3 = 1.15$, corresponds to a single ellipticity chosen for all the beams in Ring 3. Marginal variations in hot-spot symmetry and neutron yield relative to symmetric drive are modeled in Figs. 130.13(a) and 130.13(b), respectively.

Warm implosions offer the advantage that frequent, highly repeatable experiments can be conducted to study the relevant coronal physics. A warm CH, PD implosion design also predicts good performance relative to symmetric drive with the same set of beam profiles (Fig. 130.14). As in the cryogenic design, ring energies are varied [Fig. 130.14(a)] to minimize hot-spot distortion [Fig 130.14(b)]. Polar-drive–implosion velocity is very close to the symmetric-drive velocity as shown by the similar bang times between the two simulations [Fig. 130.14(c)].

Effect of Cross-Beam Transfer and Nonlocal Heat Transport in Symmetric and Polar Drives

As mentioned earlier, CBET has been invoked to explain the observed delay in bang time between experiment and simulation for symmetric-drive implosions.[10] The role of CBET in PD implosions is unclear. Experiments to measure scattered light in PD geometry and efforts to model CBET in *DRACO* are ongoing. Similar to symmetric drive, a delay in bang time is observed in warm OMEGA implosion experiments in PD geometry (Fig. 130.15). Bang time is delayed by ~180 ps in PD experiments relative to PD simulations [Fig. 130.15(a)]. This delay is similar for the various PD configurations and also similar to the delay observed for symmetric drive [Fig. 130.15(b)]. CBET's dependence on beam obliquity is also unclear. Apart from an overall delay in the absolute time, observations of shell asymmetry agree with simulations.[29] The latest time at which these measurements can be made is still relatively early, when the shell has converged by a factor of ~7. It is therefore unclear if CBET preferentially compromises laser-energy absorption at some latitudes relative to others. All the 60-beam symmetric designs presented in this article are sensitive to the model of cross-beam transfer[10] and nonlocal transport[13] implemented in *LILAC*. The implosion velocity is reduced by approximately 10% and neutron yield by approximately a factor of 3 when effects of cross-beam transfer are included in *LILAC* simulations. Areal density is also reduced by nearly 10% primarily due to the introduction of a coasting phase in the implosion caused by the driving pressure not being retained until the onset
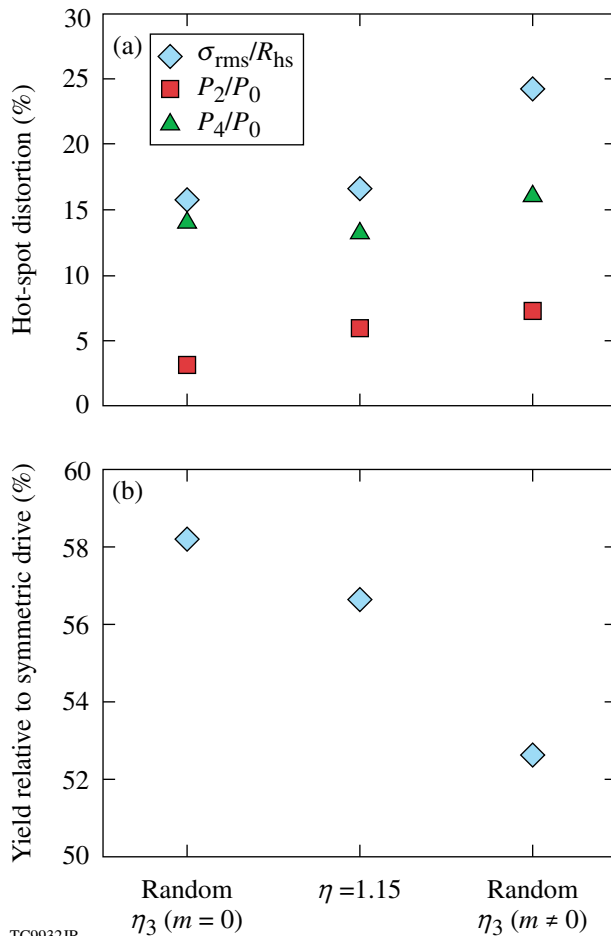

Figure 130.13
(a) Hot-spot distortion for varying ellipticities for each beam in Ring 3. Random ellipticities correspond to a randomly selected ellipticity for each beam in Ring 3 with η_3 varying uniformly between 1.1 and 1.2. Such a variation of ellipticities results in a breakdown of azimuthal symmetry. This is modeled by including only the $m = 0$ modes in the Legendre decomposition of the asymmetry in the 2-D axisymmetric simulation. The middle point, $\eta = 1.15$, corresponds to a single ellipticity chosen for all the beams in Ring 3. The third set of points corresponds to the inclusion of the amplitude of the $m \neq 0$ modes in quadrature in the amplitude of the Legendre mode used in the simulation. (b) Yield relative to symmetric drive for each of the cases in (a).

TC9932JR

of deceleration. One possible CBET mitigation strategy is to reduce the beam size relative to the target size; for example, the ratio of ~0.85 improves implosion velocity while imposing optimal levels of nonuniformity on target.[39] With the target radius selected in the previous section, the flexibility can perform such studies in PD. The high-intensity design deliberately uses only about 80% of the maximum energy available on

OMEGA; the additional 20% in laser energy is available to drive larger targets, if necessary.

Conclusions

Cryogenic-DT and warm CH polar-drive designs for the OMEGA laser have been presented. Given the available energy on OMEGA, it is challenging to get both ignition-relevant
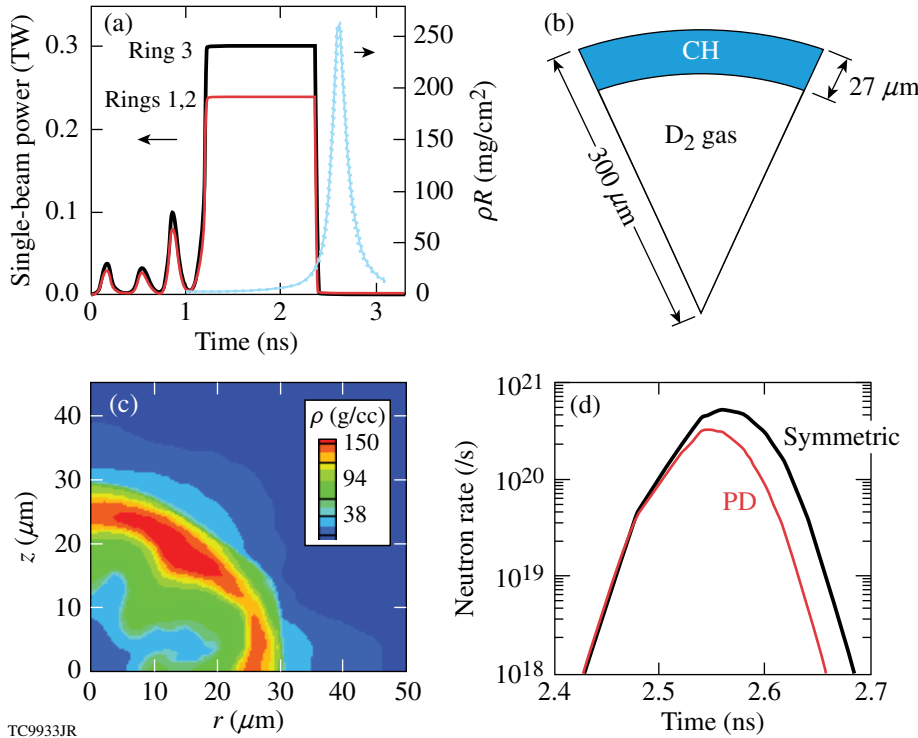

Figure 130.14

(a) Ring pulse shapes (left axis) and areal-density history (right axis) for (b) a warm, plastic-shell target. (c) Mass-density contours at peak neutron production (2.56 ns). (d) Neutron-rate histories for symmetric drive (black) compared to the PD simulation (red). No delay in bang time is observed, indicating that the symmetric-drive–implosion velocity is achieved in the PD simulation.
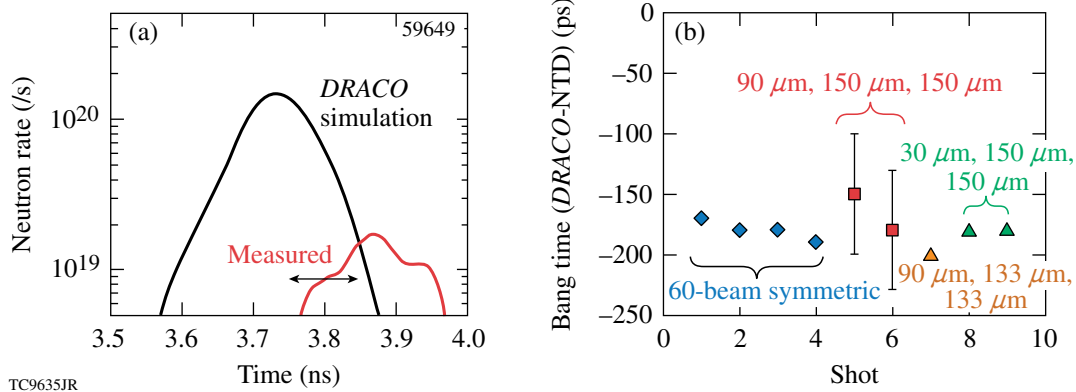

Figure 130.15

(a) Comparison of neutron rates between the measured (red) and the simulated (black) with only collisional absorption and flux-limited heat conduction values in PD configuration. (b) Difference in the simulated and measured bang times for symmetric drive and three different PD configurations. Bang time occurs earlier in the simulations when only collisional absorption of the laser pulse is assumed.

intensity (to study LPI effects and heat conduction) and high in-flight aspect ratio (to study effects of instability growth) in one design. Instead, two designs have been presented, each of which addressed one issue. A low-intensity optimized PD cryogenic DT design using the existing OMEGA phase plates predicts ~27% of the symmetric-drive yield. This yield reduction is due to reduced implosion velocity in PD relative to symmetric drive and the dominant $\ell = 4$ nonuniformity. These predictions are similar to observations from warm CH implosions on OMEGA, where a similar modal nonuniformity is observed and simulated. The observed warm implosion PD yield is reduced relative to spherically symmetric implosion experiments and is due to an inferred loss of ~10% in implosion velocity. High-intensity cryogenic and warm CH designs with smaller targets for future PD experiments on OMEGA have been presented. These designs repoint beams less by making a judicious choice of beam profiles and beam energies, permitting adequate symmetry while reducing the extent of repointed beams. Simulations indicate the recovery of symmetric-drive–implosion velocity in these designs. Weak sensitivity of target performance such as neutron yield and hot-spot distortion on beam profile parameters indicate that the designs are robust. Measurements from current OMEGA PD experiments also indicate an additional loss of ~10% in implosion velocity relative to PD simulations that include only collisional absorption as the mechanism of laser-energy deposition and flux-limited heat conduction. This reduction in implosion velocity is similar to that observed in symmetric drive, where it has been attributed to cross-beam transfer. Mitigation options include reducing the beam size relative to target radius. The beam profile radii chosen for the high-intensity design presented in this article will permit such mitigation studies by varying the target radii. Detailed experimental studies and code development to model the effect of cross-beam transfer in PD geometry are ongoing. Implosion results from the combined set of implosions should yield valuable data to develop and validate models of laser-energy deposition, heat conduction, nonuniformity growth, and fuel assembly in PD geometry.

ACKNOWLEDGEMENT

REFERENCES

1. S. Skupsky, J. A. Marozas, R. S. Craxton, R. Betti, T. J. B. Collins, J. A. Delettrez, V. N. Goncharov, P. W. McKenty, P. B. Radha, T. R. Boehly, J. P. Knauer, F. J. Marshall, D. R. Harding, J. D. Kilkenny, D. D. Meyerhofer, T. C. Sangster, and R. L. McCrory, Phys. Plasmas **11**, 2763 (2004).

2. E. Moses, presented at The Seventh International Conference on Inertial Fusion Sciences and Applications, Bourdeaux-Lac, France, 12–16 September 2011.

3. J. Nuckolls *et al.*, Nature **239**, 139 (1972).

4. T. J. B. Collins, J. A. Marozas, K. S. Anderson, R. Betti, R. S. Craxton, J. A. Delettrez, V. N. Goncharov, D. R. Harding, F. J. Marshall, R. L. McCrory, D. D. Meyerhofer, P. W. McKenty, P. B. Radha, A. Shvydky, S. Skupsky, and J. D. Zuegel, Phys. Plasmas **19**, 056308 (2012).

5. M. C. Herrmann, M. Tabak, and J. D. Lindl, Nucl. Fusion **41**, 99 (2001).

6. J. D. Lindl, *Inertial Confinement Fusion: The Quest for Ignition and Energy Gain Using Indirect Drive* (Springer-Verlag, New York, 1998).

7. S. E. Bodner, Phys. Rev. Lett. **33**, 761 (1974); H. Takabe *et al.*, Phys. Fluids **28**, 3676 (1985); R. Betti, V. N. Goncharov, R. L. McCrory, and C. P. Verdon, Phys. Plasmas **5**, 1446 (1998).

8. P. B. Radha, C. Stoeckl, V. N. Goncharov, J. A. Delettrez, D. H. Edgell, J. A. Frenje, I. V. Igumenshchev, J. P. Knauer, J. A. Marozas, R. L. McCrory, D. D. Meyerhofer, R. D. Petrasso, S. P. Regan, T. C. Sangster, W. Seka, and S. Skupsky, Phys. Plasmas **18**, 012705 (2011).

9. C. D. Zhou and R. Betti, Phys. Plasmas **14**, 072703 (2007).

10. I. V. Igumenshchev, D. H. Edgell, V. N. Goncharov, J. A. Delettrez, A. V. Maximov, J. F. Myatt, W. Seka, A. Shvydky, S. Skupsky, and C. Stoeckl, Phys. Plasmas **17**, 122708 (2010).

11. A. Simon, R. W. Short, E. A. Williams, and T. Dewandre, Phys. Fluids **26**, 3107 (1983).

12. W. Seka, D. H. Froula, D. H. Edgell, J. F. Myatt, R. W. Short, I. V. Igumenshchev, V. N. Goncharov, and A. V. Maximov, Bull. Am. Phys. Soc. **56**, 327 (2011); V. N. Goncharov, T. C. Sangster, R. Epstein, S. X. Hu, I. V. Igumenshchev, D. H. Froula, R. L. McCrory, D. D. Meyerhofer, P. B. Radha, W. Seka, S. Skupsky, C. Stoeckl, D. T. Casey, J. A. Frenje, and R. D. Petrasso, Bull. Am. Phys. Soc. **56**, 240 (2011).

13. V. N. Goncharov, T. C. Sangster, P. B. Radha, R. Betti, T. R. Boehly, T. J. B. Collins, R. S. Craxton, J. A. Delettrez, R. Epstein, V. Yu. Glebov, S. X. Hu, I. V. Igumenshchev, J. P. Knauer, S. J. Loucks, J. A. Marozas, F. J. Marshall, R. L. McCrory, P. W. McKenty, D. D. Meyerhofer, S. P. Regan, W. Seka, S. Skupsky, V. A. Smalyuk, J. M. Soures, C. Stoeckl, D. Shvarts, J. A. Frenje, R. D. Petrasso, C. K. Li, F. Séguin, W. Manheimer, and D. G. Colombant, Phys. Plasmas **15**, 056310 (2008).

14. R. Kishony and D. Shvarts, Phys. Plasmas **8**, 4925 (2001).

15. S. W. Haan, J. D. Lindl, D. A. Callahan, D. S. Clark, J. D. Salmonson, B. A. Hammel, L. J. Atherton, R. C. Cook, M. J. Edwards, S. Glenzer, A. V. Hamza, S. P. Hatchett, M. C. Herrmann, D. E. Hinkel, D. D. Ho, H. Huang, O. S. Jones, J. Kline, G. Kyrala, O. L. Landen, B. J. MacGowan, M. M. Marinak, D. D. Meyerhofer, J. L. Milovich, K. A. Moreno, E. I. Moses, D. H. Munro, A. Nikroo, R. E. Olson, K. Peterson, S. M. Pollaine, J. E. Ralph, H. F. Robey, B. K. Spears, P. T. Springer, L. J. Suter, C. A. Thomas, R. P. Town, R. Vesey, S. V. Weber, H. L. Wilkens, and D. C Wilson, Phys. Plasmas **18**, 051001 (2011).

16. T. C. Sangster, V. N. Goncharov, D. H. Edgell, D. H. Froula, V. Yu. Glebov, D. R. Harding, S. X. Hu, F. J. Marshall, R. L. McCrory, P. W. McKenty, D. D. Meyerhofer, J. F. Myatt, P. B. Radha, W. Seka, C. Stoeckl, B. Yaakobi, J. A. Frenje, M. G. Johnson, and R. D. Petrasso, Bull. Am. Phys. Soc. **56**, 241 (2011).

17. S. P. Obenschain *et al.*, Phys. Plasmas **9**, 2234 (2002).

18. T. R. Boehly, D. L. Brown, R. S. Craxton, R. L. Keck, J. P. Knauer, J. H. Kelly, T. J. Kessler, S. A. Kumpan, S. J. Loucks, S. A. Letzring, F. J. Marshall, R. L. McCrory, S. F. B. Morse, W. Seka, J. M. Soures, and C. P. Verdon, Opt. Commun. **133**, 495 (1997).

19. P. B. Radha, V. N. Goncharov, T. J. B. Collins, J. A. Delettrez, Y. Elbaz, V. Yu. Glebov, R. L. Keck, D. E. Keller, J. P. Knauer, J. A. Marozas, F. J. Marshall, P. W. McKenty, D. D. Meyerhofer, S. P. Regan, T. C. Sangster, D. Shvarts, S. Skupsky, Y. Srebro, R. P. J. Town, and C. Stoeckl, Phys. Plasmas **12**, 032702 (2005).

20. F. J. Marshall, J. A. Delettrez, R. Epstein, R. Forties, V. Yu. Glebov, J. H. Kelly, T. J. Kessler, J. P. Knauer, P. W. McKenty, S. P. Regan, V. A. Smalyuk, C. Stoeckl, J. A. Frenje, C. K. Li, R. D. Petrasso, and F. H. Séguin, Bull. Am. Phys. Soc. **48**, 56 (2003).

21. *LLE Review Quarterly Report* **65**, 1, Laboratory for Laser Energetics, University of Rochester, Rochester, NY, LLE Document No. DOE/ SF/19460-117, NTIS Order No. DE96011927 (1995).

22. R. A. Forties and F. J. Marshall, Rev. Sci. Instrum. **76**, 073505 (2005).

23. T. R. Boehly, D. H. Munro, P. M. Celliers, R. E. Olson, D. G. Hicks, V. N. Goncharov, G. W. Collins, H. F. Robey, S. X. Hu, J. A. Marozas, T. C. Sangster, O. L. Landen, and D. D. Meyerhofer, Phys. Plasmas **16**, 056302 (2009).

24. F. H. Séguin, C. K. Li, J. A. Frenje, D. G. Hicks, K. M. Green, S. Kurebayashi, R. D. Petrasso, J. M. Soures, D. D. Meyerhofer, V. Yu. Glebov, P. B. Radha, C. Stoeckl, S. Roberts, C. Sorce, T. C. Sangster, M. D. Cable, K. Fletcher, and S. Padalino, Phys. Plasmas **9**, 2725 (2002).

25. C. Stoeckl, R. E. Bahr, B. Yaakobi, W. Seka, S. P. Regan, R. S. Craxton, J. A. Delettrez, R. W. Short, J. Myatt, A. V. Maximov, and H. Baldis, Phys. Rev. Lett. **90**, 235002 (2003).

26. R. A. Lerche, D. W. Phillion, and G. L. Tietbohl, Rev. Sci. Instrum. **66**, 933 (1995).

27. W. Seka, D. H. Edgell, J. P. Knauer, J. F. Myatt, A. V. Maximov, R. W. Short, T. C. Sangster, C. Stoeckl, R. E. Bahr, R. S. Craxton, J. A. Delettrez, V. N. Goncharov, I. V. Igumenshchev, and D. Shvarts, Phys. Plasmas **15**, 056312 (2008).

28. F. J. Marshall, P. W. McKenty, J. A. Delettrez, R. Epstein, J. P. Knauer, V. A. Smalyuk, J. A. Frenje, C. K. Li, R. D. Petrasso, F. H. Séguin, and R. C. Mancini, Phys. Rev. Lett. **102**, 185004 (2009).

29. P. B. Radha, F. J. Marshall, T. R. Boehly, T. J. B. Collins, R. S. Craxton, R. Epstein, V. N. Goncharov, J. A. Marozas, R. L. McCrory, P. W. McKenty, D. D. Meyerhofer, T. C. Sangster, A. Shvydky, S. Skupsky, J. A. Frenje, and R. D. Petrasso, presented at the 7th International Conference on Inertial Fusion Sciences and Applications, Bordeaux, France, 12–16 September 2011.

30. J. A. Marozas, F. J. Marshall, R. S. Craxton, I. V. Igumenshchev, S. Skupsky, M. J. Bonino, T. J. B. Collins, R. Epstein, V. Yu. Glebov, D. Jacobs-Perkins, J. P. Knauer, R. L. McCrory, P. W. McKenty, D. D. Meyerhofer, S. G. Noyes, P. B. Radha, T. C. Sangster, W. Seka, and V. A. Smalyuk, Phys. Plasmas **13**, 056311 (2006).

31. J. Delettrez, R. Epstein, M. C. Richardson, P. A. Jaanimagi, and B. L. Henke, Phys. Rev. A **36**, 3926 (1987).

32. V. N. Goncharov, T. C. Sangster, T. R. Boehly, S. X. Hu, I. V. Igumenshchev, F. J. Marshall, R. L. McCrory, D. D. Meyerhofer, P. B. Radha, W. Seka, S. Skupsky, C. Stoeckl, D. T. Casey, J. A. Frenje, and R. D. Petrasso, Phys. Rev. Lett. **104**, 165001 (2010).

33. C. Stoeckl, P. B. Radha, R. E. Bahr, J. A. Delettrez, D. H. Edgell, V. Yu. Glebov, V. N. Goncharov, I. V. Igumenshchev, T. C. Sangster, W. Seka, J. A. Frenje, and R. D. Petrasso, Bull. Am. Phys. Soc. **56**, 241 (2011).

34. S. Skupsky, R. W. Short, T. Kessler, R. S. Craxton, S. Letzring, and J. M. Soures, J. Appl. Phys. **66**, 3456 (1989).

35. T. R. Boehly, V. A. Smalyuk, D. D. Meyerhofer, J. P. Knauer, D. K. Bradley, R. S. Craxton, M. J. Guardalben, S. Skupsky, and T. J. Kessler, J. Appl. Phys. **85**, 3444 (1999).

36. R. Betti and C. Zhou, Phys. Plasmas **12**, 110702 (2005).

37. T. C. Sangster, V. N. Goncharov, P. B. Radha, V. A. Smalyuk, R. Betti, R. S. Craxton, J. A. Delettrez, D. H. Edgell, V. Yu. Glebov, D. R. Harding, D. Jacobs-Perkins, J. P. Knauer, F. J. Marshall, R. L. McCrory, P. W. McKenty, D. D. Meyerhofer, S. P. Regan, W. Seka, R. W. Short, S. Skupsky, J. M. Soures, C. Stoeckl, B. Yaakobi, D. Shvarts, J. A. Frenje, C. K. Li, R. D. Petrasso, and F. H. Séguin, Phys. Rev. Lett. **100**, 185006 (2008).

38. P. B. Radha, J. P. Knauer, T. C. Sangster, V. N. Goncharov, I. V. Igumenshchev, R. Betti, R. Epstein, D. D. Meyerhofer, and S. Skupsky, Bull. Am. Phys. Soc. **52**, 143 (2007).

39. D. H. Froula, B. Yaakobi, S. X. Hu, P.-Y. Chang, R. S. Craxton, D. H. Edgell, R. Follett, D. T. Michel, J. F. Myatt, W. Seka, R. W. Short, A. Solodov, and C. Stoeckl, Phys. Rev. Lett. **108**, 165003 (2012).